

Optimizing Binding Energies of Key Intermediates for CO₂ Hydrogenation to Methanol over Oxide-Supported Copper

Shyam Kattel,^{†,#} Binhang Yan,^{†,‡,#} Yixiong Yang,[§] Jinguang G. Chen,^{*,†,||} and Ping Liu^{*,†}

[†]Chemistry Department, Brookhaven National Laboratory, Upton, New York 11973, United States

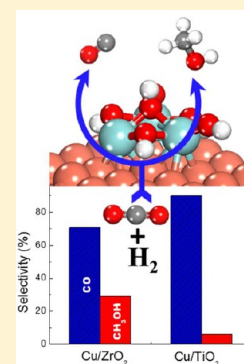
[‡]Department of Chemical Engineering, Tsinghua University, Beijing 100084, China

[§]Chemistry Department, Stony Brook University, Stony Brook, New York 11794, United States

^{||}Department of Chemical Engineering, Columbia University, New York, New York 10027, United States

S Supporting Information

ABSTRACT: Rational optimization of catalytic performance has been one of the major challenges in catalysis. Here we report a bottom-up study on the ability of TiO₂ and ZrO₂ to optimize the CO₂ conversion to methanol on Cu, using combined density functional theory (DFT) calculations, kinetic Monte Carlo (KMC) simulations, in situ diffuse reflectance infrared Fourier transform spectroscopy (DRIFTS) measurements, and steady-state flow reactor tests. The theoretical results from DFT and KMC agree with in situ DRIFTS measurements, showing that both TiO₂ and ZrO₂ help to promote methanol synthesis on Cu via carboxyl intermediates and the reverse water–gas-shift (RWGS) pathway; the formate intermediates, on the other hand, likely act as a spectator eventually. The origin of the superior promoting effect of ZrO₂ is associated with the fine-tuning capability of reduced Zr³⁺ at the interface, being able to bind the key reaction intermediates, e.g. *CO₂, *CO, *HCO, and *H₂CO, moderately to facilitate methanol formation. This study demonstrates the importance of synergy between theory and experiments to elucidate the complex reaction mechanisms of CO₂ hydrogenation for the realization of a better catalyst by design.



1. INTRODUCTION

Metal-oxide catalysts are widely used as catalysts to facilitate many important processes.^{1–3} Extensive efforts have been made to provide mechanistic understanding of the variation in catalytic properties on going from metal to metal/oxide catalysts. The special synergy between metals and oxides can reflect large electronic perturbations in the metals,^{4,5} introduce special sites at the metal/oxide interface,^{1,6–10} and induce the structural variation of metal nanostructures,^{11,12} which directly affect the bonding strength of the catalyst and therefore the catalytic performances. The present study aims to provide fundamental insight into the effect of varying oxide supports on the catalysis of metal-oxide catalysts, using a combination of density functional theory (DFT) calculations, kinetic Monte Carlo (KMC) simulations, in situ diffuse reflectance infrared Fourier transform spectroscopy (DRIFTS) measurements, and steady-state flow reactor experiments. Carbon dioxide (CO₂) hydrogenation to methanol on Cu/oxide catalysts was taken as a case study.

The CO₂ concentration in the atmosphere has severe impact on global climate change and ocean acidification. The conversion of CO₂ to chemicals, e.g. carbon monoxide (CO) and methanol (CH₃OH), represents one of the potential ways to reduce the CO₂ level and has attracted enormous attention in recent years.^{1,13–28} Industrially, the CH₃OH synthesis from CO₂ hydrogenation is conducted over a Cu/ZnO/Al₂O₃ catalyst at 220–300 °C.²⁹ Even though the reaction is exothermic, the conversion of CO₂ to CH₃OH is kinetically

limited to 15–25% at elevated pressures of 50–100 atm.^{1,30} Significant efforts have been devoted to improving the catalytic performance of the Cu-based catalysts. An enhancement in CO₂ conversion and CH₃OH selectivity was achieved by forming Cu alloys,^{31,32} and using reducible metal oxides as support for Cu. Among the Cu/oxides studied, ZrO₂^{33–35} and TiO₂^{1,36,37} are very promising catalyst supports and/or promoters. However, little has been done on mechanistic comparison of the catalytic performance of Cu/ZrO₂ and Cu/TiO₂ using both theory and experiment, where the catalysts are synthesized and tested under comparable conditions. Furthermore, the origin of the promoting effects of TiO₂ and ZrO₂ on the catalytic performance of Cu toward CO₂ hydrogenation is not well understood at the molecular level. Both ZrO₂ and TiO₂ are reducible and likely adopt similar structures. Understanding their different behaviors in modifying the catalysis of Cu will help in optimizing the performance of metal/oxide catalysts.

The present combined study is a detailed mechanistic comparison of the catalytic performances of metal oxides introduced by various oxides, where the catalytic CO₂ hydrogenation on Cu/TiO₂ and Cu/ZrO₂ was extensively studied in terms of activity, selectivity, and stability. Both DFT calculations and the in situ DRIFTS measurements demonstrate that Cu/TiO₂ and Cu/ZrO₂ promote the CO₂

Received: June 6, 2016

Published: August 29, 2016

hydrogenation to CH₃OH via the reverse water–gas-shift (RWGS) reaction to produce CO followed by its hydrogenation to CH₃OH through the formation of methoxy (*H₃CO) as a reaction intermediate, while the formate (*HCOO) species are likely spectators and poison the active sites on the surface. A superior performance of ZrO₂ over TiO₂ is observed in both theory and steady-state flow reactor experiments for promoting the overall conversion and CH₃OH selectivity of Cu during CO₂ hydrogenation. According to the detailed mechanistic study, the synergistic interaction between Cu and reduced Zr³⁺ ions at the metal/oxide interface is able to increase the binding properties of Cu to facilitate CO₂ conversion to CH₃OH, but not too much to generate poisoning of active sites by adsorbates.

2. METHODS

2.1. Computational Methods. Spin-polarized density functional theory (DFT)^{38,39} calculations were carried out using the Vienna *ab initio* simulation package (VASP)⁴⁰ code. The generalized gradient approximation of Perdew and Wang (PW91)⁴¹ was employed for the electronic exchange and correlation. The plane wave pseudopotential with a kinetic cutoff energy of 400 eV within the projector augmented wave (PAW)^{42,43} method was used. The Gaussian smearing method with an electronic temperature of $k_B T = 0.05$ eV was employed to obtain faster convergence. The Cu(111) surface was modeled by a four-layer 5 × 5 unit cell. The bottom two layers in the unit cell were fixed in their optimized bulk positions while the top two layers along with the metal-oxide clusters were allowed to relax until the forces were below 0.02 eV/Å. The Brillouin-zone integration was performed on a grid of 3 × 3 × 1 Monkhorst–Pack⁴⁴ special k-points. A vacuum layer of 20 Å thick was applied perpendicular to the slab to avoid artificial interactions between the slab and its periodic images. The electronic structure of Ti was treated in the DFT + U⁴⁵ formalism with a U value of 4.5 eV.^{46,47} The transition state of a chemical reaction was located using the climbing image nudged elastic band (CI-NEB) method implemented in VASP.⁴⁸ The activation energy (E_a) of a chemical reaction is defined as the energy difference between the initial and transition states while the reaction energy (ΔE) is defined as the energy difference between the initial and final states.

An inverse model was used to determine the effect of the oxide support on the activity of Cu toward CO₂ hydrogenation, where the oxide clusters were deposited on the Cu(111) surface. Such an inverse model has been recently shown to be appropriate to describe the catalytic properties of Cu/oxide catalysts under CO₂ hydrogenation conditions.^{1,49} It is able to capture the structural motif at the metal/oxide interface, which plays a key role in promoting the activity.^{50–53} The metal-oxide cluster adsorption energy (ΔE_{ads}) on the Cu(111) surface is defined as

$$\Delta E_{\text{ads}} = E[\text{metal-oxide cluster/Cu(111)}] - E[\text{Cu(111)}] - E[\text{metal-oxide cluster(g)}]$$

where $E[\text{metal-oxide cluster/Cu(111)}]$, $E[\text{Cu(111)}]$, and $E[\text{metal-oxide cluster(g)}]$ are the total energies of optimized Cu(111) with the metal-oxide cluster, the clean Cu(111) surface, and the metal-oxide cluster in the gas phase, respectively. Similarly, the binding energy (BE) of an adsorbate on the metal-oxide/Cu(111) surface is defined as

$$\text{BE(adsorbate)} = E(\text{adsorbate} + \text{metal-oxide/Cu(111)}) - E(\text{metal-oxide/Cu(111)}) - E(\text{adsorbate})$$

where $E(\text{adsorbate} + \text{metal-oxide/Cu(111)})$, $E(\text{metal-oxide/Cu(111)})$ and $E(\text{adsorbate})$ are the total energies of optimized adsorbate + metal-oxide/Cu(111), clean metal-oxide/Cu(111), and adsorbate in the gas phase, respectively.

2.2. Experimental Methods. **2.2.1. Catalysts Synthesis.** The Cu/ZrO₂ and Cu/TiO₂ catalysts were synthesized by deposition–precipitation on commercial supports (ZrO₂ with a surface area of

90 m²/g, and TiO₂ (anatase) with a surface area larger than 150 m²/g, from Alfa Aesar). The supports were dried for 12 h at 100 °C before Cu deposition. The Cu precursor (Cu(NO₃)₂·3H₂O from Sigma-Aldrich) and 200 mL of distilled water were added to a beaker under stirring to form a 8 mM Cu(NO₃)₂ solution. Then, urea (CO(NH₂)₂ from Sigma-Aldrich) was added to the solution in a concentration 100 times of Cu(NO₃)₂ at room temperature. Afterward, the preweighed support was added to the beaker and the solution was heated to 80 °C at a heating rate of 1 °C/min to make urea slowly hydrolyze, homogeneously producing ammonium hydroxide through the solution. Since an effective mixing is very important, the solution was stirred vigorously for 5 h. The solution pH gradually rose to about 7.6 at the beginning and then remained practically constant. The Cu loading of the catalysts in this work was 5 wt %. After the deposition–precipitation step, the solution was filtered and washed with 200 mL of distilled water three times. The recovered samples were dried at 90 °C for 12 h and then calcined in air at 350 °C for 4 h with a heating rate of 0.8 °C/min.

2.2.2. In-Situ DRIFTS Measurements. In-situ DRIFTS measurements were performed in order to detect and characterize the surface adsorbates and reaction intermediates over Cu/ZrO₂ and Cu/TiO₂ catalyst under reaction conditions. The spectra were collected using a FTIR spectrometer (Thermo, Nicolet 6700) equipped with a MCT detector. Before measurement, each catalyst was reduced in a hydrogen/helium mixture (10 mL/min hydrogen with 10 mL/min helium) at 350 °C for 30 min, and then purged with a 20 mL/min He at 360 °C for 20 min. Subsequently, the catalyst was cooled down to 235 °C (i.e., reaction temperature). The background spectrum (256 scans) with a resolution of 4 cm⁻¹ was obtained at 235 °C in He flow (20 mL/min). The in situ DRIFT spectra during the CO₂ hydrogenation reaction at 235 °C were recorded by collecting 64 scans at 4 cm⁻¹ resolution, according to the following procedure after the pretreatment: (1) the sample (Cu/ZrO₂ or Cu/TiO₂) was exposed to a CO₂/helium mixture (5 mL/min CO₂ with 15 mL/min helium) at 235 °C for 10 min; (2) the CO₂ hydrogenation reaction was then conducted with a CO₂/hydrogen mixture (5 mL/min CO₂ with 15 mL/min hydrogen) for 30 min; (3) the reaction cell was purged with a 20 mL/min helium for 30 min. The in situ DRIFT spectra shown in this work were expressed in units of Kubelka–Monk, in which only bands attributed to adsorbed species were shown.

2.2.3. Steady-State Flow Reactor Testing. Flow reactor studies for CO₂ hydrogenation under atmospheric pressure were carried out in a quartz tube reactor at 220 °C. The powder catalysts (40–80 mesh) were reduced under a 1:1 hydrogen and argon mixture (40 mL/min total flow rate) at 350 °C for 1 h prior to reaction. The flow rates of CO₂ and hydrogen were set at 10 and 30 mL/min, respectively. For each experiment, the temperature was ramped to 220 °C and held for over 12 h until the reaction was under steady-state. The products at the reactor outlet were detected with an online gas chromatographer (Agilent 7890B) equipped with a thermal conductivity detector (TCD) and a flame ionization detector (FID).

3. RESULTS AND DISCUSSION

3.1. Mechanistic Studies of CO₂ Hydrogenation Using DFT and KMC. Two major reaction pathways have been proposed for CO₂ hydrogenation over Cu,^{32,54–61} as illustrated in Figure 1. The first pathway is featured by the CO intermediate, which is produced from the reverse-water–gas-shift (RWGS: CO₂ + H₂ → CO + H₂O) reaction via carboxyl (*HOCO) species and is further hydrogenated to the final product CH₃OH (designated as the CO-Hydro pathway); the other pathway is associated with the formate (*HCOO) intermediate formed by CO₂ hydrogenation, which eventually produces CH₃OH via the C–O bond cleavage and *HCO or *H₂CO intermediates (designated as the Formate pathway).⁶² In the present study, the mechanistic study of CO₂ hydrogenation on Cu/oxides was carried out using self-consistent periodic DFT calculations. By adapting an inverse model, which

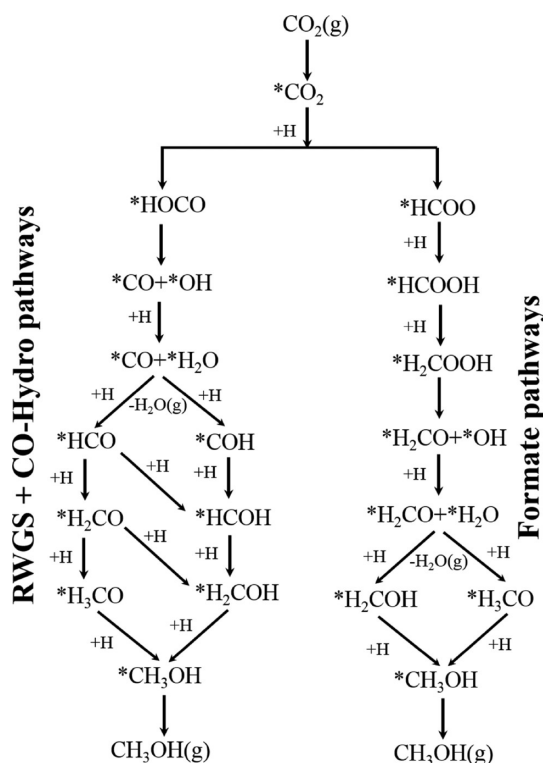


Figure 1. Reaction scheme for $\text{CO}_2(\text{g})$ hydrogenation to $\text{CH}_3\text{OH}(\text{g})$ via the RWGS + CO-Hydro and Formate pathways. $^*(\text{X})$ indicates adsorbed species.

has been shown to be a reasonable model for describing the catalytic properties of metal–oxide catalysts under CO_2 hydrogenation conditions,¹ the Cu/oxides interface is modeled by depositing small oxide clusters Ti_3O_6 and Zr_3O_6 on the Cu(111) surface. Although the oxide trimmers may be too small to describe those observed in the experiment, they are likely to resemble the low coordinated sites and structural flexibility of the interfacial oxides. Such small oxide cluster was successfully employed to describe the experimentally observed trend in activity toward CO_2 hydrogenation on metal/oxide catalysts.⁶³ In addition, H_2 dissociation on the Cu(111) surface is facile,⁶⁴ yet the dissociated $^*\text{H}$ is not stable on Cu and recombines to desorb as H_2 . With the presence of the oxide cluster on Cu(111), $^*\text{H}$ favors the spillover to the O atoms of the oxide clusters to form OH groups. These results agree well with previous studies, where the spillover of H from metal particles to oxide supports including TiO_2 and ZrO_2 was clearly detected experimentally.⁶⁵ Therefore, the hydroxylation of oxide clusters was considered and the Cu/oxide interface was modeled by depositing hydroxylated Ti_3O_6 and Zr_3O_6 clusters, i.e., $\text{Ti}_3\text{O}_6\text{H}_6$ and $\text{Zr}_3\text{O}_6\text{H}_6$ clusters on the Cu(111) surface as shown in Figure 2.

3.1.1. Hydroxylated $\text{Ti}_3\text{O}_6/\text{Cu}(111)$. The $\text{Ti}_3\text{O}_6\text{H}_6/\text{Cu}(111)$ system was constructed with all six O atoms of the Ti_3O_6 cluster saturated by H atoms (Figure 2a). As a result, O atoms saturated by H atoms no longer interact with the Cu(111) surface. Instead, the $\text{Ti}_3\text{O}_6\text{H}_6$ cluster is anchored to Cu(111) only through Ti–Cu bonds and tilted by $\sim 45^\circ$ to the Cu(111) surface, while the binding energy (-3.14 eV) is only slightly weakened (-3.36 eV for $\text{Ti}_3\text{O}_6/\text{Cu}(111)$). According to Bader charge analysis, there is a $\sim +1$ e shift going from Ti in $\text{Ti}_3\text{O}_6\text{H}_6/\text{Cu}(111)$, which directly interacts with Cu(111) and is identified to be active for the reaction as seen in the

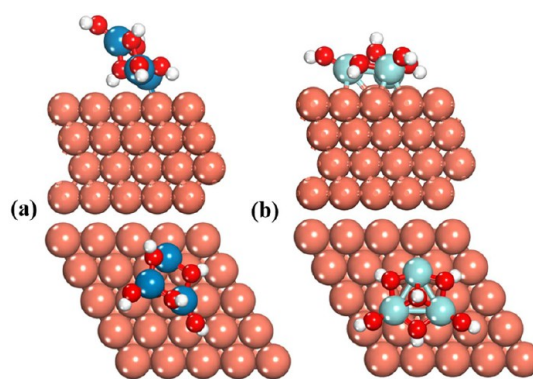


Figure 2. DFT optimized geometries: top (side view), bottom (top view) of (a) $\text{Ti}_3\text{O}_6\text{H}_6/\text{Cu}(111)$ and (b) $\text{Zr}_3\text{O}_6\text{H}_6/\text{Cu}(111)$. Cu: reddish-orange, Ti: dark blue, Zr: light blue, O: red, and H: white.

following, to Ti in rutile TiO_2 bulk. This suggests that active Ti has an oxidation state of +3.

To obtain insights into the reaction pathways, the intermediates, and the rate limiting steps, the potential energy diagrams of the catalytic $\text{CO}_2(\text{g})$ hydrogenation to $\text{CH}_3\text{OH}(\text{g})$ on $\text{Ti}_3\text{O}_6\text{H}_6/\text{Cu}(111)$ were calculated, where both the RWGS + CO-Hydro and Formate pathways were included. It is evident that the metal-oxide interfacial sites directly participate in binding and stabilizing most of the reaction intermediates: $^*\text{CO}_2$, $^*\text{HOCO}$, $^*\text{CO}$, $^*\text{HCO}$, $^*\text{H}_2\text{CO}$, $^*\text{HCOH}$, and $^*\text{H}_2\text{COH}$ species via $\eta^2\text{-C}_{\text{Cu}}\text{O}_{\text{Ti}^{3+}}$ as well as $^*\text{HCOO}$, $^*\text{H}_2\text{COOH}$, and $^*\text{OH}$ via $\eta^2\text{-O}_{\text{Cu}}\text{O}_{\text{Ti}^{3+}}$. Only four of the reaction intermediates, $^*\text{H}_3\text{CO}$, $^*\text{HCOOH}$, $^*\text{H}_2\text{O}$, and $^*\text{CH}_3\text{OH}$, interact with the Ti^{3+} sites of $\text{Ti}_3\text{O}_6\text{H}_6$ via $\eta^1\text{-O}_{\text{Ti}^{3+}}$ (Figure 3 and Table 1).

The reaction starts with CO_2 adsorption at the $\text{Ti}_3\text{O}_6\text{H}_6/\text{Cu}(111)$ interfacial sites in a bent configuration, where the C atom sits on Cu and one of the O atoms interacts with Ti (BE = -0.32 eV, Figure 3a). In comparison, on unmodified Cu(111), CO_2 stays in a linear configuration, such as that in the gas phase.³¹ This difference indicates that CO_2 is activated by depositing TiO_2 on Cu, which forms carboxylate species ($^*\text{CO}_2^-$) and can promote the overall CO_2 conversion. Along the RWGS + CO-Hydro pathway (Figure 4), $^*\text{CO}_2$ hydrogenation leads to the formation of $^*\text{HOCO}$ ($\Delta E = 0.07$, $E_a = 0.89$ eV), which dissociates into $^*\text{CO}$ and $^*\text{OH}$ ($\Delta E = -0.20$, $E_a = 0.68$ eV). $^*\text{OH}$ is hydrogenated to form $^*\text{H}_2\text{O}$ ($\Delta E = -0.12$, $E_a = 0.61$ eV). $^*\text{CO}$ produced via the RWGS reaction either desorbs by overcoming a barrier of 1.21 eV, or undergoes hydrogenation to $^*\text{HCO}$ ($\Delta E = 0.47$ eV, $E_a = 0.73$ eV); however, the entropic contribution under the reaction conditions significantly lowers the barrier for CO desorption, e.g. by ~ 1 eV at 220 °C. Therefore, it is likely that CO is the major product for CO_2 hydrogenation on $\text{Ti}_3\text{O}_6\text{H}_6/\text{Cu}(111)$, while only a small amount of $^*\text{CO}$ is available for further hydrogenation to $^*\text{HCO}$, $^*\text{H}_2\text{CO}$ ($\Delta E = -0.23$ eV, $E_a = 0.54$ eV), $^*\text{H}_3\text{CO}$ ($\Delta E = -0.86$ eV, $E_a = 0.14$ eV), and the final product $^*\text{CH}_3\text{OH}$ ($\Delta E = -0.08$ eV, $E_a = 0.77$ eV). In addition, there is another obstacle to hinder the CH_3OH yield, besides the preferential CO desorption. As shown in Figure 4, although the formation ($E_a = 0.73$ eV) and the hydrogenation ($E_a = 0.54$ eV) of $^*\text{HCO}$ are not highly activated, both steps cannot compete with its decomposition to $^*\text{CO}$ ($E_a = 0.26$ eV). It suggests that $^*\text{HCO}$ is not stable and prefers to decompose back to produce $^*\text{CO}$.

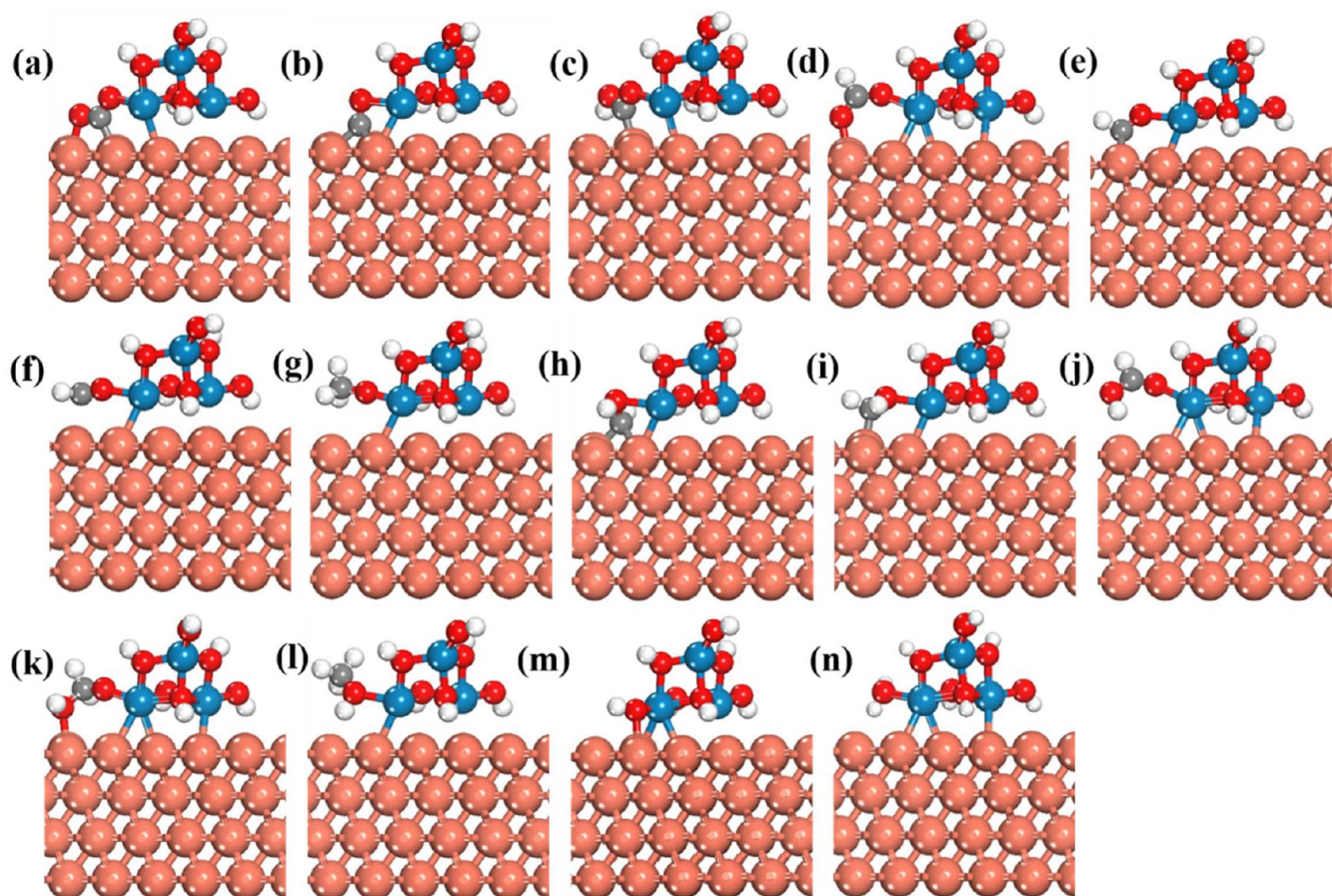


Figure 3. DFT optimized geometries. (a) $^*\text{CO}_2$, (b) $^*\text{CO}$, (c) $^*\text{HOCO}$, (d) $^*\text{HCOO}$, (e) $^*\text{HCO}$, (f) $^*\text{H}_2\text{CO}$, (g) $^*\text{H}_3\text{CO}$, (h) $^*\text{HCOH}$, (i) $^*\text{H}_2\text{COH}$, (j) $^*\text{HCOOH}$, (k) $^*\text{H}_2\text{COOH}$, (l) $^*\text{CH}_3\text{OH}$, (m) $^*\text{OH}$, and (n) $^*\text{H}_2\text{O}$ on $\text{Ti}_3\text{O}_6\text{H}_6/\text{Cu}(111)$. Cu: reddish-orange, Ti: blue, O: red, C: gray, and H: white.

Table 1. Binding Energies (BE in eV) of Chemical Species Involved in CH_3OH Synthesis from CO_2 Hydrogenation via the RWGS + CO-Hydro and Formate Pathways

Species	Binding site	$\text{Ti}_3\text{O}_6\text{H}_6/\text{Cu}(111)$	Binding site	$\text{Zr}_3\text{O}_6\text{H}_6/\text{Cu}(111)$
H	$\eta^1\text{-H}_{\text{Cu}}$	-2.51	$\eta^1\text{-H}_{\text{Cu}}$	-2.52
CO_2	$\eta^2\text{-C}_{\text{Cu}}\text{O}_{\text{Ti}\delta^+}$	-0.32	$\eta^2\text{-C}_{\text{Cu}}\text{O}_{\text{Zr}\delta^+}$	-1.18
OH	$\eta^2\text{-C}_{\text{Cu}}\text{O}_{\text{Ti}\delta^+}$	-3.70	$\eta^1\text{-O}_{\text{Zr}\delta^+}$	-5.00
H_2O	$\eta^1\text{-O}_{\text{Ti}\delta^+}$	-0.83	$\eta^1\text{-O}_{\text{Zr}\delta^+}$	-0.99
CO	$\eta^2\text{-C}_{\text{Cu}}\text{O}_{\text{Ti}\delta^+}$	-1.21	$\eta^2\text{-C}_{\text{Cu}}\text{O}_{\text{Zr}\delta^+}$	-1.86
HOCO	$\eta^2\text{-C}_{\text{Cu}}\text{O}_{\text{Ti}\delta^+}$	-2.37	$\eta^2\text{-C}_{\text{Cu}}\text{O}_{\text{Zr}\delta^+}$	-3.10
HCOO	$\eta^2\text{-O}_{\text{Cu}}\text{O}_{\text{Ti}\delta^+}$	-3.46	$\eta^2\text{-O}_{\text{Cu}}\text{O}_{\text{Zr}\delta^+}$	-4.18
HCO	$\eta^2\text{-C}_{\text{Cu}}\text{O}_{\text{Ti}\delta^+}$	-2.07	$\eta^2\text{-C}_{\text{Cu}}\text{O}_{\text{Zr}\delta^+}$	-2.91
HCOH	$\eta^2\text{-C}_{\text{Cu}}\text{O}_{\text{Ti}\delta^+}$	-2.43		
H_2CO	$\eta^2\text{-C}_{\text{Cu}}\text{O}_{\text{Ti}\delta^+}$	-0.82	$\eta^2\text{-C}_{\text{Cu}}\text{O}_{\text{Zr}\delta^+}$	-2.07
H_2COH	$\eta^2\text{-C}_{\text{Cu}}\text{O}_{\text{Ti}\delta^+}$	-1.70		
H_3CO	$\eta^1\text{-O}_{\text{Ti}\delta^+}$	-3.01	$\eta^1\text{-O}_{\text{Zr}\delta^+}$	-4.41
HCOOH	$\eta^1\text{-O}_{\text{Ti}\delta^+}$	-0.76	$\eta^1\text{-O}_{\text{Zr}\delta^+}$	-1.19
H_2COOH	$\eta^2\text{-O}_{\text{Cu}}\text{O}_{\text{Ti}\delta^+}$	-2.89	$\eta^1\text{-O}_{\text{Zr}\delta^+}$	-4.25
CH_3OH	$\eta^1\text{-O}_{\text{Ti}\delta^+}$	-0.88	$\eta^1\text{-O}_{\text{Zr}\delta^+}$	-1.10

Along the Formate pathway (Figure 4), the initial hydrogenation of $^*\text{CO}_2$ to $^*\text{HCOO}$ is exothermic ($\Delta E = -0.63$ eV, $E_a = 0.46$ eV). $^*\text{HCOO}$ then undergoes hydrogenation to form $^*\text{HCOOH}$ ($\Delta E = 0.30$ eV, $E_a = 0.85$ eV) and then $^*\text{H}_2\text{COOH}$ ($\Delta E = 0.01$ eV, $E_a = 0.67$ eV). $^*\text{H}_2\text{COOH}$ is the precursor for C–O bond cleavage, which produces $^*\text{H}_2\text{CO}$ ($\Delta E = 0.57$ eV,

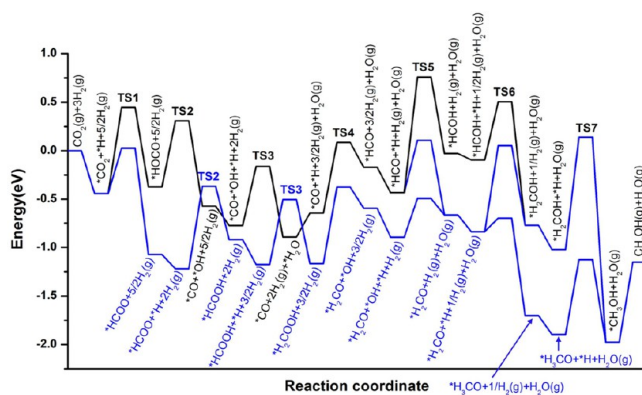


Figure 4. Potential energy diagrams for the hydrogenation of $\text{CO}_2(\text{g})$ to $\text{CH}_3\text{OH}(\text{g})$ on $\text{Ti}_3\text{O}_6\text{H}_6/\text{Cu}(111)$ via the RWGS + CO-Hydro and Formate pathways. “TS” corresponds to the transition state.

$E_a = 0.79$ eV) and finally $^*\text{CH}_3\text{OH}$ via a similar route to that in the CO-Hydro pathway. The $^*\text{CO}_2$ hydrogenation to $^*\text{HCOO}$ is more facile than that to $^*\text{HOCO}$ ($E_a = 0.89$ eV), suggesting the preference of the Formate pathway over the RWGS + CO-Hydro pathway. However, the stability of $^*\text{H}_2\text{CO}$ is rather low along the Formate pathway. The formation of $^*\text{H}_2\text{CO}$ via $^*\text{H}_2\text{COOH}$ decomposition ($E_a = 0.79$ eV) is much less favorable than the reverse reaction ($E_a = 0.22$ eV). As a result, the CH_3OH yield should be limited, as the $^*\text{HCOO}$ species

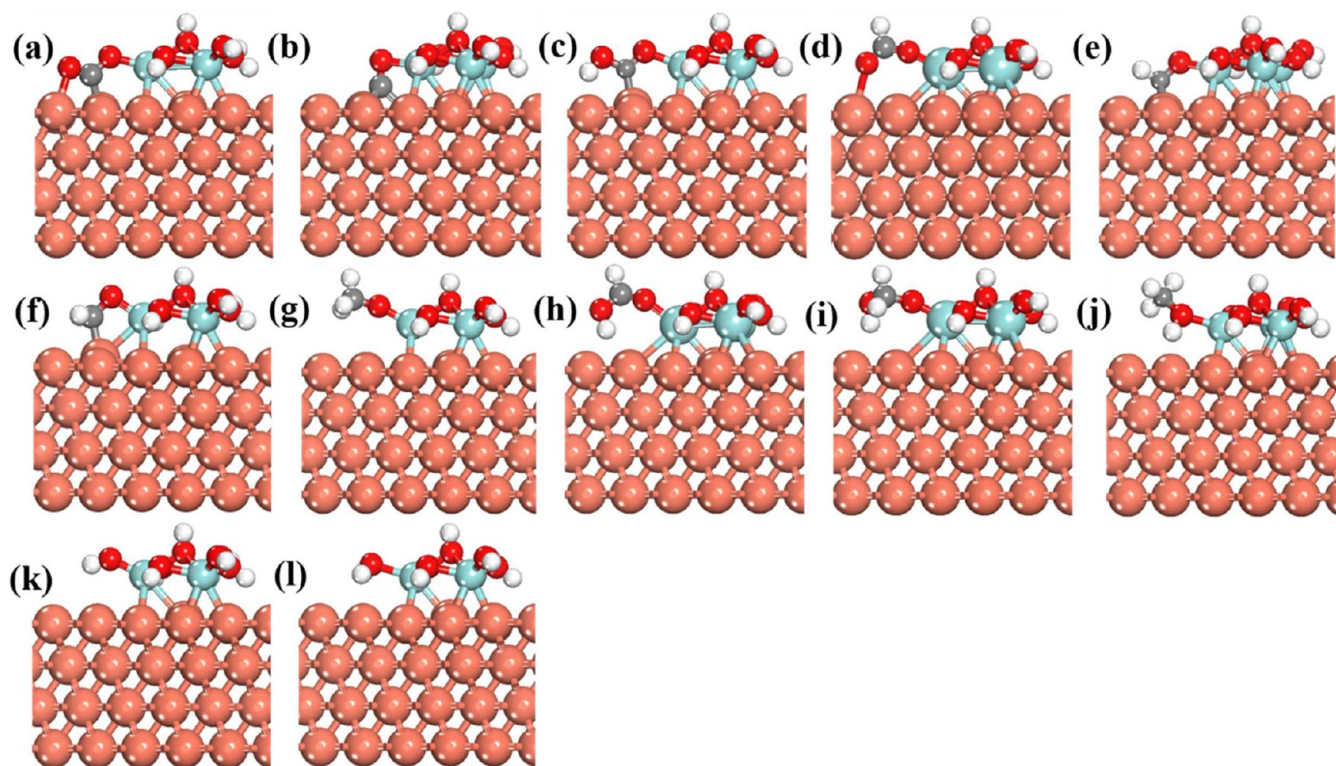


Figure 5. DFT optimized geometries. (a) $^*\text{CO}_2$, (b) $^*\text{CO}$, (c) $^*\text{HOCO}$, (d) $^*\text{HCOO}$, (e) $^*\text{HCO}$, (f) $^*\text{H}_2\text{CO}$, (g) $^*\text{H}_3\text{CO}$, (h) $^*\text{HCOOH}$, (i) $^*\text{H}_2\text{COOH}$, (j) $^*\text{CH}_3\text{OH}$, (k) $^*\text{OH}$, and (l) $^*\text{H}_2\text{O}$ on $\text{Zr}_3\text{O}_6\text{H}_6/\text{Cu}(111)$. Cu: reddish-orange, Zr: light blue, O: red, C: gray, and H: white.

likely accumulate on the surface and does not contribute to the overall production of CH_3OH .

According to the DFT calculations, the deposition of TiO_2 is able to promote the CO_2 adsorption and therefore the overall CO_2 conversion on Cu; however, the effect is relatively small on the selective production of CH_3OH , and CO likely remains as the major product. Along the RWGS + CO-Hydro pathway, the low stability of the intermediates, such as $^*\text{CO}$, $^*\text{HCO}$, or $^*\text{H}_2\text{CO}$, hinders the complete conversion of CO_2 to CH_3OH , rather resulting in the partial hydrogenation to CO, while the highly stable $^*\text{HCOO}$ species along the Formate pathway likely leads to surface poisoning.

3.1.2. Hydroxylated $\text{Zr}_3\text{O}_6\text{H}_6/\text{Cu}(111)$. $\text{Zr}_3\text{O}_6\text{H}_6$ adopts similar structures as $\text{Ti}_3\text{O}_6\text{H}_6$, where a +1 e shift in the Bader charge is also observed going from Zr in $\text{Zr}_3\text{O}_6\text{H}_6/\text{Cu}(111)$, which is active to bond with O-containing species as shown in the following, to that in bulk cubic- ZrO_2 , indicating a reduction of Zr to an oxidation state equivalent to +3 by the formation of $\text{Zr}_3\text{O}_6\text{H}_6/\text{Cu}(111)$. Differently, by deposition on Cu(111), $\text{Zr}_3\text{O}_6\text{H}_6$ is in close contact with the surface via Zr^{3+} -Cu bonds (Figure 2b), rather than tilting away as $\text{Ti}_3\text{O}_6\text{H}_6$ (Figure 2a). That is, Zr^{3+} displays higher activity in binding than Ti^{3+} , as indicated by the higher density of states of Zr^{3+} near the Fermi level than Ti^{3+} (Figure S1 in the Supporting Information). For most reaction intermediates, the binding sites on $\text{Zr}_3\text{O}_6\text{H}_6/\text{Cu}(111)$ are similar to those of $\text{Ti}_3\text{O}_6\text{H}_6/\text{Cu}(111)$ (Table 1 and Figure 5). Differences are seen for $^*\text{OH}$ and $^*\text{H}_2\text{COOH}$, where the stabilization is achieved by Zr^{3+} alone. This is strongly associated with the higher binding property of Zr^{3+} than Ti^{3+} , being able to stabilize the adsorbate more in cooperation with Cu via $\eta^2\text{-C}_{\text{Cu}}\text{O}_{\text{Zr}^{3+}}$ or by itself via $\eta^1\text{-O}_{\text{Zr}^{3+}}$ (Table 1). The CO_2 binding is enhanced on $\text{Zr}_3\text{O}_6\text{H}_6/\text{Cu}(111)$ by 0.86 eV, suggesting a potentially significant enhancement in

the overall CO_2 conversion compared to $\text{Ti}_3\text{O}_6\text{H}_6/\text{Cu}(111)$. In addition, the key intermediates to control the CH_3OH selectivity on $\text{Ti}_3\text{O}_6\text{H}_6/\text{Cu}(111)$, $^*\text{CO}$, $^*\text{HCO}$, and $^*\text{H}_2\text{CO}$, are also stabilized from $\text{Ti}_3\text{O}_6\text{H}_6$ to $\text{Zr}_3\text{O}_6\text{H}_6$ (Table 1). To understand whether such stabilization promotes the CO_2 conversion to CH_3OH , the potential energy diagram was calculated in Figure 6.

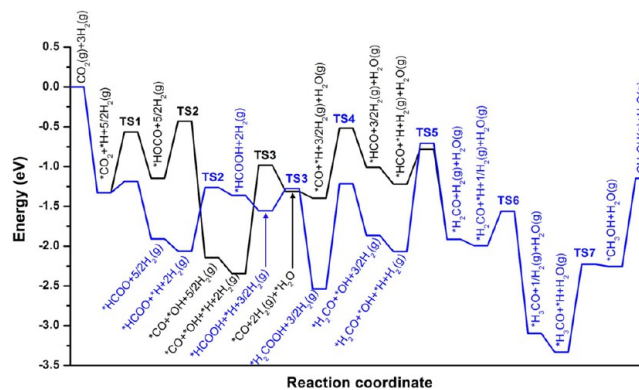


Figure 6. Potential energy diagram for the hydrogenation of $\text{CO}_2(\text{g})$ to $\text{CH}_3\text{OH}(\text{g})$ on $\text{Zr}_3\text{O}_6\text{H}_6/\text{Cu}(111)$ via the RWGS + CO-Hydro and Formate pathways. “TS” corresponds to the transition state.

Along the RWGS + CO-Hydro pathway (Figure 6), the initial hydrogenation of $^*\text{CO}_2$ to $^*\text{HOCO}$ is more favorable ($\Delta E = 0.18$ eV, $E_a = 0.76$ eV) than that of $\text{Ti}_3\text{O}_6\text{H}_6/\text{Cu}(111)$, while the dissociation to $^*\text{CO} + ^*\text{OH}$ is energetically comparable, with the difference in barrier being 0.04 eV. Different from the case of $\text{Ti}_3\text{O}_6\text{H}_6/\text{Cu}(111)$, the formation of $^*\text{H}_2\text{O}$ is highly activated ($\Delta E = 1.03$ eV, $E_a = 1.36$ eV) due to

the strong binding of OH at the $Zr_3O_6H_6/Cu(111)$ interface (Table 1). In the case of *CO , E_a for desorption (1.86 eV) is competitive with the hydrogenation to *HCO ($\Delta E = 0.39$ eV, $E_a = 0.88$ eV) on $Zr_3O_6H_6/Cu(111)$ even after including the entropy contribution. In addition, the stability of *HCO is greatly increased. Consequently, the decomposition of *HCO to *CO is less favorable ($E_a = 0.49$ eV). Finally, *HCO hydrogenation to *H_2CO ($\Delta E = -0.69$ eV, $E_a = 0.44$ eV) is slightly more preferred than *HCO decomposition. The hydrogenation of *H_2CO leads to the formation of *H_3CO ($\Delta E = -1.10$ eV, $E_a = 0.43$ eV) and then CH_3OH ($\Delta E = 1.07$ eV, $E_a = 1.11$ eV). Overall, the increased stability of *CO , *HCO , and *H_2CO on $Zr_3O_6H_6/Cu(111)$ compared to $Ti_3O_6H_6/Cu(111)$ promotes the reactions via the CO-Hydro pathway to produce CH_3OH .

The strengthened bindings in the case of $Zr_3O_6H_6/Cu(111)$ result in some drawbacks. Along the reaction channel, there are two possible bottleneck steps. One is *OH hydrogenation ($E_a = 1.36$ eV), which hinders H_2O production via the RWGS reaction; the other is *H_3CO hydrogenation ($E_a = 1.11$ eV), which slows down the CH_3OH yield. Both steps display a higher barrier on $Zr_3O_6H_6/Cu(111)$ than that on $Ti_3O_6H_6/Cu(111)$. In this case, *OH and *H_3CO are too strongly bound to react (Table 1). However, each step is followed by a facile desorption, H_2O or CH_3OH , which can drive the reaction going forward under the reaction conditions with help from entropic contributions.

Along the Formate pathway, the initial hydrogenation of *CO_2 to *HCOO ($\Delta E = -0.58$ eV, $E_a = 0.14$ eV) on $Zr_3O_6H_6/Cu(111)$ is even more facile than that on $Ti_3O_6H_6/Cu(111)$ (Figure 6), due to the increased stability of *HCOO by 0.72 eV (Table 1). The further hydrogenation to *HCOOH ($\Delta E = 0.70$ eV, $E_a = 0.80$ eV) can be hindered by the facile reverse reaction ($E_a = 0.10$ eV). In fact, the decomposition of *HCOOH to *HCOO is faster than not only the *HCOO hydrogenation, but also the rest of the steps, including hydrogenation of *HCOOH to *H_2COOH ($\Delta E = -0.98$ eV, $E_a = 0.28$ eV), *H_2COOH dissociation to *H_2CO and *OH ($\Delta E = 0.67$ eV and $E_a = 1.32$ eV), and *H_2CO hydrogenation to *CH_3OH . Therefore, the CO_2 hydrogenation on $Zr_3O_6H_6/Cu(111)$ via the Formate pathway is likely slowed down due to the highly stabilized *HCOO over time, which occupies the active sites and prevents the production of CH_3OH .

3.1.3. KMC Simulations. The KMC simulations were performed based on the DFT-calculated potential energies for CO_2 hydrogenation on $Ti_3O_6H_6/Cu(111)$ and $Zr_3O_6H_6/Cu(111)$ (Figures 4 and 6), aiming to gain a qualitative understanding of the reaction mechanism, the formation of reaction intermediates on surfaces, and the rate controlling steps. In the present work, the KMC simulations (for details see the Supporting Information, SI) were performed with a Kinetix module implemented in Material Studio 5.5.⁶⁶ For the reactions involving gases, the contribution from the entropy was included according to the NIST database.⁶⁷ The KMC simulations including the RWGS + CO-Hydro and the Formate pathways (Table S1) for CO_2 hydrogenation to CH_3OH were carried out at the experimental temperature of 220 °C for 60 s. It results in the same trend in activity and coverage of reaction intermediates as compared to that for 300 s, which approaches the steady state (Figure S2).

On both Cu/TiO_2 and Cu/ZrO_2 catalysts, *HCOO is the most abundant surface species according to the KMC simulations for the duration of 60 s (Figure S3), and the

amount kept increasing, consistent with the observation after 300 s (Figure S2). In addition, the stronger binding to *HCOO on Cu/ZrO_2 (Table 1) results in higher coverage of *HCOO species than that on Cu/TiO_2 (Figure S3). Although *H_2COOH species are also observed on Cu/ZrO_2 , the amount is much lower than *HCOO . The presence of *H_3CO on both catalysts is also observed, which displays higher coverage on Cu/ZrO_2 than on Cu/TiO_2 ; yet the corresponding coverage is lower than that of *HCOO , in particular for Cu/ZrO_2 (Figure S3).

In addition, the preferential reaction pathways can also be identified. On Cu/ZrO_2 *CO production is only via the RWGS, where about 50% desorb as CO gas and the rest undergo hydrogenation to produce CH_3OH . The Formate pathway also helps for the CH_3OH production, and the contribution from both pathways is about the same at the initial stage. However, due to the high stability of *HCOO on the surface, the kinetics of the CH_3OH production along the Formate pathway can be limited over time due to the poisoning of the catalytically active surface sites. In contrast, it is found that the reaction proceeds continuously via the RWGS + CO-Hydro pathway with no surface poisoning. Compared to Cu/ZrO_2 , Cu/TiO_2 is less selective to CH_3OH . The Formate pathway mainly results in *HCOO with a very small amount of CH_3OH produced. The RWGS reaction yields CO , while the further hydrogenation to CH_3OH is diminished compared to Cu/ZrO_2 due to weaker binding of CO and consequently more facile CO desorption. Given that, the RWGS + CO-Hydro pathway eventually should dominate the overall production of CH_3OH on both catalysts.

The sensitivity analysis, in which each parameter in the KMC model is shifted by a small amount from its original value by keeping the other parameters constant, is performed to predict the highest number of rate or selectivity controlling steps.³² In the case of Cu/ZrO_2 , four rate-controlling steps for the CH_3OH production are identified, and the yield can be promoted by facilitating *CO hydrogenation to *HCO and/or suppressing *CO desorption via the RWGS + CO-Hydro pathway; the counter variations lead to the enhancement in CO production, which can also be achieved by accelerating *CO_2 hydrogenation to *HOCO (Figure S4); by comparison, the effect associated with the *H_2COOH dissociation to *H_2CO and the *HCOO hydrogenation to *HCOOH along the Formate pathway is smaller. For Cu/TiO_2 , the small amount of CH_3OH production is dominated initially by the Formate pathway, which is very sensitive to the *HCOO activation to *HCOOH (Figure S5); yet the *HCOO species increasingly accumulate over time (Figure S2) and eventually limit the CH_3OH production. The major CO production is only limited by the CO_2 hydrogenation to *HOCO along the RWGS + CO-Hydro pathway (Figure S5).

According to sensitivity analysis, on Cu/ZrO_2 the CO binding energy is likely the descriptor to scale the CH_3OH production via the RWGS + CO-Hydro pathway. To maximize the CH_3OH yield in this case, CO binding should be moderate, being strong enough to prevent desorption, but weak enough to allow the facile hydrogenation to *HCO . Along the Formate pathway, the CH_3OH production can be effectively promoted by increasing *H_2CO binding and therefore facilitating *H_2COOH dissociation. In the case of Cu/TiO_2 , *HCOO binding is too strong, which slows down the formation of CH_3OH via the Formate pathway due to the highly activated hydrogenation. Previously, the binding energy of O on metal

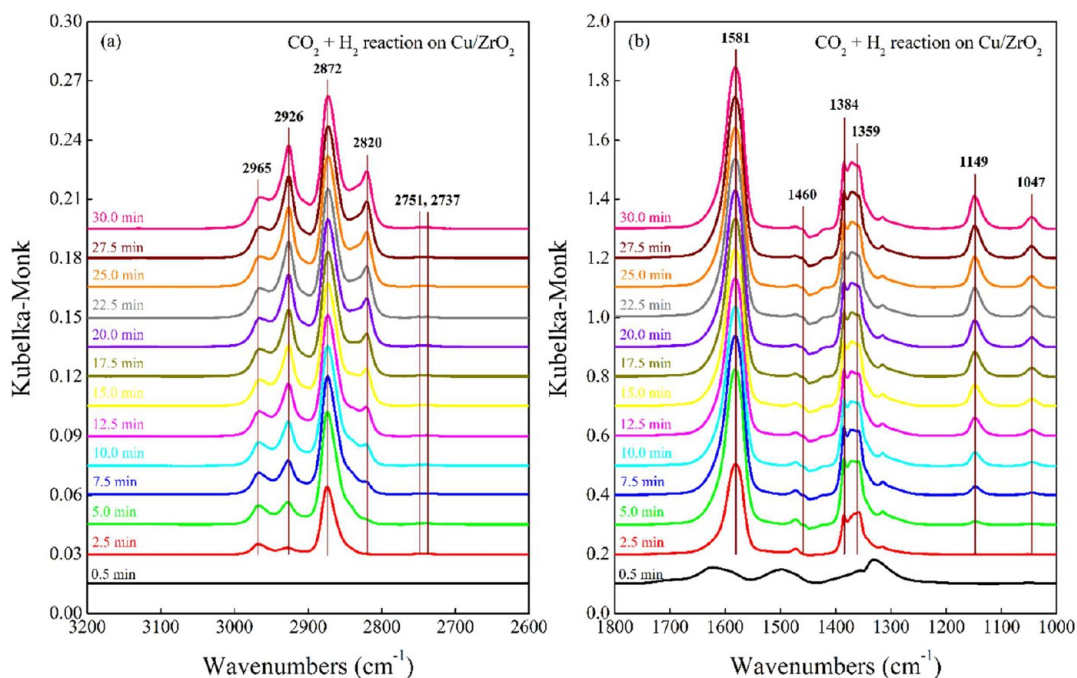


Figure 7. In-situ DRIFT spectra of the $\text{CO}_2 + \text{H}_2$ reaction after CO_2 absorption on Cu/ZrO_2 catalyst in the regions (a) $3200\text{--}2600\text{ cm}^{-1}$ and (b) $1800\text{--}1000\text{ cm}^{-1}$ (Reaction conditions: $5\text{ mL}/\text{min CO}_2 + 15\text{ mL}/\text{min H}_2$, 0.1 MPa , $235\text{ }^\circ\text{C}$).

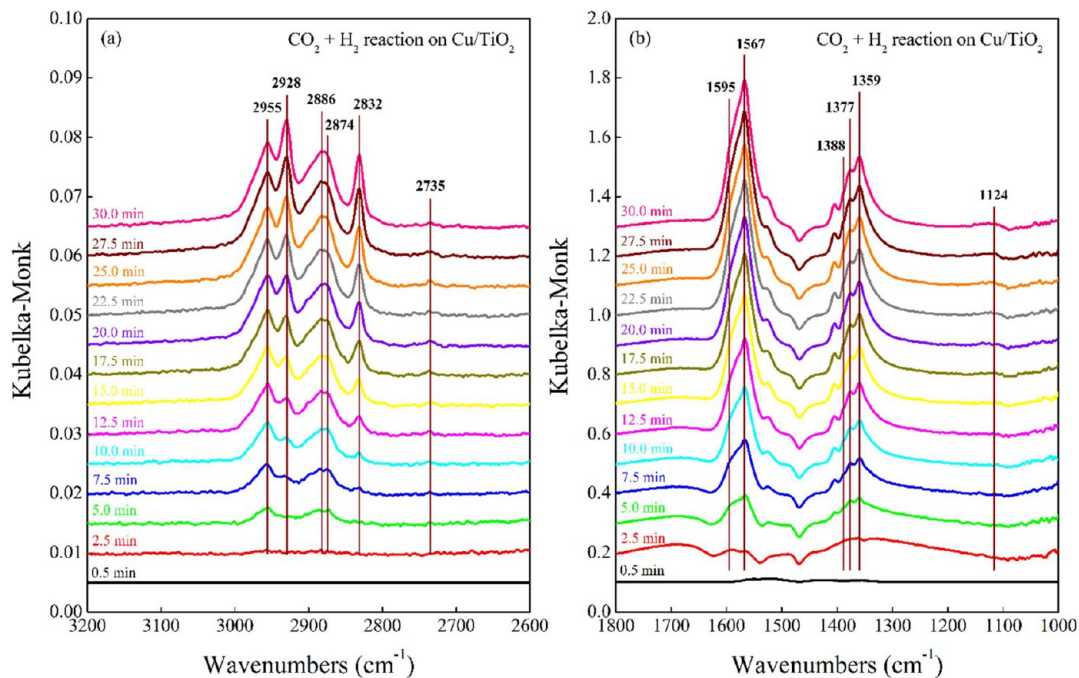


Figure 8. In-situ DRIFT spectra of the $\text{CO}_2 + \text{H}_2$ reaction after CO_2 absorption on Cu/TiO_2 catalyst in the regions (a) $3200\text{--}2600\text{ cm}^{-1}$ and (b) $1800\text{--}1000\text{ cm}^{-1}$ (Reaction conditions: $5\text{ mL}/\text{min CO}_2 + 15\text{ mL}/\text{min H}_2$, 0.1 MPa , $235\text{ }^\circ\text{C}$).

catalysts has been identified as a descriptor of selectivity between the RWGS and methanation pathways⁶⁸ on late transition metal surfaces as well as the CH_3OH selectivity on metal alloy catalysts.¹⁴ By comparison, on metal/oxide catalysts as shown in this case, the situation is more complicated. The interface provides multiple active sites to enable multiple pathways running in parallel, and the rate-controlling steps or the key intermediates vary from one pathway to the next and from one system to the next. As a result, the CH_3OH

production rate does not depend on a single descriptor or the binding energy of a common key intermediate.

The combined DFT and KMC results show general similarities between TiO_2 and ZrO_2 . Using either oxide leads to an increase in CO_2 conversion and CH_3OH production of Cu catalysts during CO_2 hydrogenation along the RWGS + CO -Hydro and the Formate pathways. Although the CO_2 hydrogenation to $^*\text{HCOO}$ is more favorable than to $^*\text{HOCO}$ along the RWGS pathway due to the highly stable $^*\text{HCOO}$ species formed on both catalysts, the accumulation of

*HCOO species on the surface occurs over time and leads to surface poisoning. By comparison, the contribution from the RWGS + CO-Hydro pathway is more practical. Different catalytic behaviors of Cu/TiO₂ and Cu/ZrO₂ are also observed. The promoting effect induced by ZrO₂ is more significant than that of TiO₂. The CO₂ conversion is increased by stronger CO₂ interaction with ZrO₂ than with TiO₂. The selectivity to CH₃OH is also raised over Cu/ZrO₂ due to the enhanced stability of the *CO, *HCO and *H₂CO intermediates, which enables the *CO hydrogenation to CH₃OH to be more competitive with CO desorption and therefore greatly increases the CH₃OH yield via the Formate and RWGS + CO-Hydro pathways. The modification introduced by ZrO₂ increases binding of Cu slightly, strongly enough to facilitate the reaction, but weakly enough to hinder the poisoning of active sites; however, along the Formate pathway the surface poisoning by *HCOO can be more severe over time by using ZrO₂ than TiO₂. To verify these theoretically predicted similarities and differences between TiO₂- and ZrO₂-supported Cu for CO₂ hydrogenation, a combination of the in situ DRIFTS measurements and steady-state flow reactor was carried out as shown in the following.

3.2. Experimental Results. 3.2.1. In-Situ DRIFTS Results.

In-situ DRIFTS experiments were performed to identify the possible intermediates during CO₂ hydrogenation over Cu/ZrO₂ and Cu/TiO₂. Figures 7 and 8 show the transient evolution of the principal surface species during CO₂ hydrogenation at 235 °C over Cu/ZrO₂ and Cu/TiO₂, respectively.

As shown in Figure 7, two surface species, *HCOO and *H₃CO, were observed and identified.^{69–74} The assignments of these absorption bands over Cu/ZrO₂ during CO₂ hydrogenation are listed in Table 2. The bands at 1581 and 1359 cm⁻¹ were assigned to the antisymmetric and symmetric OCO stretching vibrations of adsorbed bidentate *HCOO species on Cu/ZrO₂. The bands at 1384 and 2872 cm⁻¹ were assigned to the CH bending ($\delta(\text{CH})$) and stretching ($\nu(\text{CH})$) vibrations of

Table 2. Infrared Band Assignments of the Surface Species for the CO₂ + H₂ Reaction over Cu/ZrO₂ at 235 °C and Atmospheric Pressure (5 mL/min CO₂ + 15 mL/min H₂, 0.1 MPa)

Surface species	Wavenumber (cm ⁻¹)	Assignment	Literature value (cm ⁻¹)
Bidentate formate	2965	$\delta(\text{CH}) + \nu_{\text{as}}(\text{OCO})$	2969; ⁷⁴ 2975; ⁷³ 2967; ⁷² 2974 ⁷¹
	2872	$\nu(\text{CH})$	2883; ⁷⁴ 2885–2895; ⁷³ 2880; ⁷² 2892 ⁷¹
	2751, 2737	$\delta(\text{CH}) + \nu_{\text{s}}(\text{OCO})$	2745; ⁷⁴ 2740 ⁷²
	1581	$\nu_{\text{as}}(\text{OCO})$	1563; ⁷⁴ 1562; ⁷³ 1580; ⁷² 1565 ⁷¹
	1384	$\delta(\text{CH})$	1386; ⁷⁴ 1390; ⁷³ 1381; ⁷² 1386 ⁷¹
	1359	$\nu_{\text{s}}(\text{OCO})$	1366; ⁷⁴ 1370; ⁷³ 1360; ⁷² 1369 ⁷¹
Methoxy	2926	$\nu_{\text{as}}(\text{CH}_3)$	2936; ⁷⁴ 2936; ⁷³ 2942; ⁷¹ 2930 ⁷⁰
	2820	$\nu_{\text{s}}(\text{CH}_3)$	2836; ⁷⁴ 2837; ⁷³ 2842; ⁷¹ 2825 ⁷⁰
	1460	$\nu(\text{CH})$	1474; ⁷⁴ 1463; ⁷¹ 1460 ⁷⁰
	1149	$\nu(\text{CO})$ of bridged (b-OCH ₃)	1142; ⁷⁴ 1150; ⁷³ 1144; ⁷⁰ 1154 ⁶⁹
	1047	$\nu(\text{CO})$ of terminal (t-OCH ₃)	1039; ⁷⁴ 1052 ⁶⁹

the same species. The feature at 2965 cm⁻¹ was attributed to a combination of the CH bending and asymmetric OCO stretching modes. The bands at 2926 and 2820 cm⁻¹ were attributed to the $\nu(\text{CH}_3)$ modes of the *H₃CO species on Cu/ZrO₂, while the features at 1149 and 1047 cm⁻¹ were assigned to the $\nu(\text{CO})$ modes of bridged and terminal methoxide species, respectively.

For CO₂ hydrogenation over Cu/TiO₂, besides *HCOO and *H₃CO, *CO₂ species were also observed, as shown in Figure 8. The assignments of these vibrational features are listed in Table 3.^{75–81} The $\nu_{\text{as}}(\text{OCO})$ at 1567 cm⁻¹ and $\nu_{\text{s}}(\text{OCO})$ at 1359 cm⁻¹ were contributed by both *H₃CO and *CO₂ species on Cu/TiO₂.

Table 3. Infrared Band Assignments of the Surface Species for CO₂ + H₂ Reaction on Cu/TiO₂ at 235 °C and Atmospheric Pressure (5 mL/min CO₂ + 15 mL/min H₂, 0.1 MPa)

Surface species	Wavenumber (cm ⁻¹)	Assignment	Literature value (cm ⁻¹)
Bidentate formate	2955	$\delta(\text{CH}) + \nu_{\text{as}}(\text{OCO})$	2955; ⁸¹ 2958; ⁸⁰ 2956 ⁷⁹
	2886, 2874	$\nu(\text{CH})$	2875; ⁸¹ 2880; ⁸⁰ 2883, 2874 ⁷⁹
	2735	$\delta(\text{CH}) + \nu_{\text{s}}(\text{OCO})$	2739 ⁸¹
	1567	$\nu_{\text{as}}(\text{OCO})$	1560; ⁸¹ 1568, 1555; ⁸⁰ 1560, 1558 ⁷⁹
	1388	$\delta(\text{CH})$	1381; ⁷⁸ 1388 ⁷⁷
	1359	$\nu_{\text{s}}(\text{OCO})$	1360; ⁸¹ 1370, 1360; ⁸⁰ 1359, 1351 ⁷⁹
Methoxy	2928	$\nu_{\text{as}}(\text{CH}_3)$	2925; ⁸¹ 2930; ⁸⁰ 2923 ⁷⁶
	2832	$\nu_{\text{s}}(\text{CH}_3)$	2820; ⁸¹ 2835; ⁸⁰ 2817 ⁷⁶
	1124	$\nu(\text{CO})$	1128 ⁷⁶
Carboxylate	1595, 1567	$\nu_{\text{as}}(\text{OCO})$	1595, 1569; ⁷⁹ 1570–1630 ⁷⁵
	1377, 1359	$\nu_{\text{s}}(\text{OCO})$	1382, 1355; ⁷⁹ 1350–1390 ⁷⁵

The observations for the IR agree well with the KMC predictions (Figure S3). As shown in Figure 9, the IR peaks at 2872 and 2820 cm⁻¹ were used to follow the concentration changes of *HCOO and *H₃CO species on Cu/ZrO₂, respectively, while the bands at 2886 and 2832 cm⁻¹ were used to follow these two species on Cu/TiO₂, respectively. For the CO₂ + H₂ reaction over Cu/ZrO₂, the surface bidentate *HCOO species are populated rapidly by introducing H₂ to the reaction cell and reaching a steady-state level after approximately 5 min. The intensity of the *H₃CO species on Cu/ZrO₂ becomes apparent after 5 min and then continues to increase but reaches a stable value after 30 min. As a comparison, that for surface bidentate *HCOO species on Cu/TiO₂ increases gradually after the introduction of H₂ and reaching to a steady-state level after 30 min. The *H₃CO species on Cu/TiO₂ are barely visible until 7.5 min, and then increase linearly with time. The only difference is that the *H₂COOH species observed on Cu/ZrO₂ in KMC simulations are not detected by IR. This can be due to the fact that the amount of *H₂COOH is much lower than *HCOO.

It can be seen from Figure 9 that the formation rate of *H₃CO does not rely on the formation rate of *HCOO. In agreement with the KMC results, this suggests that the reaction do not occur via the Formate pathway for both catalysts. *HCOO and *H₃CO species on Cu/ZrO₂ are clearly much more than that on Cu/TiO₂, though the amount of OCO species on both catalysts is almost the same according to the

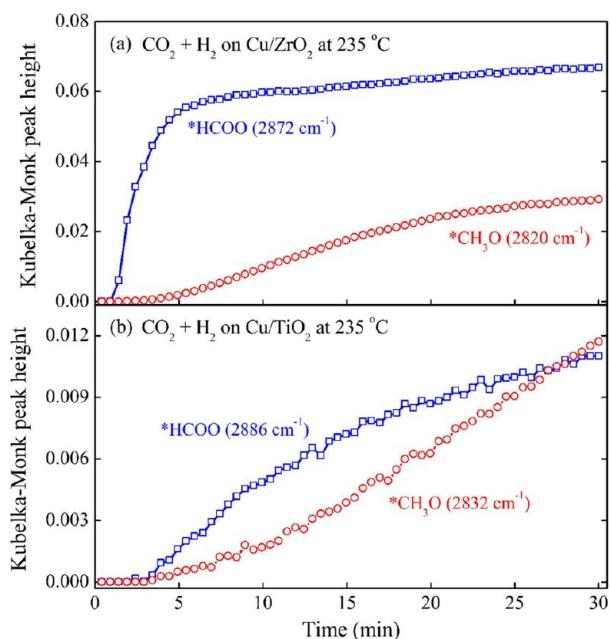


Figure 9. IR peak intensities of surface formate and methoxy species versus time during $\text{CO}_2 + \text{H}_2$ reaction over (a) Cu/ZrO_2 and (b) Cu/TiO_2 catalysts. (Reaction conditions: 5 mL/min $\text{CO}_2 + 15$ mL/min H_2 , 0.1 MPa, 235 °C).

peak intensity of the vibrational bands attributed to $\nu_{\text{as}}(\text{OCO})$ and $\nu_{\text{s}}(\text{OCO})$ modes (Figures 7 and 8). Besides, the formation rates of $^*\text{HCOO}$ and $^*\text{H}_3\text{CO}$ species on Cu/ZrO_2 are much larger than that on Cu/TiO_2 , indicating that Cu/ZrO_2 is more effective in CO_2 activation and CH_3OH formation.

3.2.2. Steady-State Flow Reactor Results. The CO_2 hydrogenation on Cu/ZrO_2 and Cu/TiO_2 catalysts was further evaluated in a fixed bed flow reactor at 220 °C. The steady-state conversion, the ratio of CH_3OH to CO , and the corresponding space–time yield to CH_3OH over the two catalysts with the same weight (approximately 100 mg) are listed in Table 4.

Table 4. CO_2 and H_2 Conversions and CH_3OH and CO Space–Time Yields over Cu/ZrO_2 and Cu/TiO_2 Catalysts with the Same Catalyst Weight (reaction conditions: 220 °C, 10 mL/min $\text{CO}_2 + 30$ mL/min H_2 , 100 mg catalyst)

Catalyst	Cu/ZrO_2	Cu/TiO_2
CO_2 conversion (%)	0.80	0.15
H_2 conversion (%)	0.39	0.08
$\text{CH}_3\text{OH}:\text{CO}$ ratio (–)	0.29	0.27
Space–time yield ($\text{g}_{\text{CO}} \text{kg}_{\text{cata}}^{-1} \text{h}^{-1}$)	42.41	7.89
Space–time yield ($\text{g}_{\text{MeOH}} \text{kg}_{\text{cata}}^{-1} \text{h}^{-1}$)	13.84	2.45

Under similar reaction conditions, the CO_2 and H_2 conversions over Cu/ZrO_2 are much higher than those over Cu/TiO_2 . Due to the weak adsorption of hydrogen and CO over the Cu/ZrO_2 and Cu/TiO_2 catalysts, it is not possible to determine the numbers of active sites from hydrogen or CO chemisorption, which would be required to estimate the turnover frequency (TOF) values. Instead, the space–time yield to CH_3OH is used to compare the activities of these two catalysts, showing that Cu/ZrO_2 is more active for CO_2 hydrogenation and CH_3OH production. In order to compare the selectivity of these two catalysts at a similar CO_2 conversion, the experiments with less amount of Cu/ZrO_2 and more amount of Cu/TiO_2 under the

same reaction conditions were performed. The total flow rate of reactants was changed in order to vary the space–time while the volume ratio of H_2 to CO_2 was kept at 3:1. As summarized in Table 5, the selectivity and space–time yield to CH_3OH on Cu/ZrO_2 are much higher than those on Cu/TiO_2 for each case, suggesting that CH_3OH formation is more favorable on Cu/ZrO_2 . More details regarding the relationship between selectivity and conversion are provided in the SI (Figure S6). Therefore, the flow reactor results also indicate that Cu/ZrO_2 presents better activity and selectivity for CH_3OH production than Cu/TiO_2 .

Overall, the theoretical calculations and the corresponding experiments using in situ DRIFTS and the steady-state flow reactor are consistent. Although the quantitative comparison between theory and experiment cannot be conducted due to the complexity of the catalysts, qualitative agreement can be reached. Both TiO_2 and ZrO_2 were found to modify the reaction mechanism on Cu , where the reaction prefers to follow the Formate pathway, according to the previous study.⁸² The mechanistic studies based on DFT and KMC simulations agree with the in situ DRIFTS measurements, showing that the RWGS + CO -Hydro pathway via the $^*\text{H}_3\text{CO}$ intermediate is likely dominate for CH_3OH synthesis on Cu/TiO_2 and Cu/ZrO_2 . Furthermore, the theory-predicted trend in activity and selectivity is verified by the experiments using the steady-state flow reactor, where ZrO_2 is more effective than TiO_2 in enhancing the activity and CH_3OH selectivity on Cu . Upon going from Cu/TiO_2 to Cu/ZrO_2 , the CO_2 conversion is facilitated due to the fine-tuning capability of ZrO_2 , being strong enough to stabilize $^*\text{CO}_2$, $^*\text{CO}$, $^*\text{HCO}$, and $^*\text{H}_2\text{CO}$ at the Cu/ZrO_2 interface and therefore promote its hydrogenation to CH_3OH via the RWGS + CO -Hydro pathway, but weak enough to prevent the poisoning of active sites. The Formate pathway produces $^*\text{HCOO}$ species, which are too stable and limit the conversion to CH_3OH . As $^*\text{HCOO}$ species are more stable on Cu/ZrO_2 than Cu/TiO_2 , more severe $^*\text{HCOO}$ accumulation on Cu/ZrO_2 is expected during the reaction, consistent with the in situ DRIFTS results. Ideally, to achieve further improvement for CO_2 hydrogenation, the modified Cu should provide additional stabilization selectively to species such as $^*\text{CO}_2$, $^*\text{CO}$, $^*\text{HCO}$, and $^*\text{H}_2\text{CO}$ to facilitate the CH_3OH yield via the RWGS + CO -Hydro pathway. Of course, one also has to avoid the over-stabilization, which can result in complete C–O bond cleavage and $^*\text{C}$ condensation; at the meantime the bindings of the $^*\text{HCOO}$ species should be weakened to release the surface poisoning and promote the contributions of CH_3OH formation via the Formate pathway. Our results highlight that the combination of DFT calculations, KMC simulations, and experimental measurements is essential to provide significant insight into the complex reaction mechanisms, such as CO_2 hydrogenation to CH_3OH . Although the current study focuses on comparing the trend in activity and selectivity between theory and experiments, additional theoretical studies to provide a quantitative comparison will be an important area for future research.

4. CONCLUSIONS

DFT and KMC simulations were combined with in situ experimental measurements to study the reaction mechanism of CO_2 hydrogenation to CH_3OH on Cu/TiO_2 and Cu/ZrO_2 catalysts, aiming to set a mechanistic comparison of catalysis on metal/oxide systems and gain a better understanding of the capability of different reducible oxides in tuning activity and

Table 5. Selectivity and Space–Time Yield to CH₃OH and CO of Cu/ZrO₂ and Cu/TiO₂ Catalysts at Similar Conversions (reaction conditions: 220 °C, CO₂:H₂:N₂ = 1:3:1, 30 mg Cu/ZrO₂, 400 mg Cu/TiO₂)

Total flow rate (mL/min)	Catalyst	Conversion (%)		Selectivity (%)		Space–time yield (g kg _{cat} ⁻¹ h ⁻¹)	
		CO ₂	H ₂	CO	CH ₃ OH	CO	CH ₃ OH
37.5	Cu/ZrO ₂	0.53	0.24	80.2	19.8	78.8	22.3
	Cu/TiO ₂	0.54	0.23	83.6	13.8	5.8	1.1
50	Cu/ZrO ₂	0.43	0.21	78.3	21.7	83.3	26.4
	Cu/TiO ₂	0.44	0.19	81.9	15.7	6.1	1.3
62.5	Cu/ZrO ₂	0.37	0.18	76.0	24.0	86.7	31.3
	Cu/TiO ₂	0.36	0.17	80.3	17.3	6.1	1.5
75	Cu/ZrO ₂	0.32	0.16	75.6	24.4	89.9	33.2
	Cu/TiO ₂	0.31	0.15	79.3	18.2	6.3	1.7
87.5	Cu/ZrO ₂	0.29	0.15	73.0	27.0	92.1	38.9
	Cu/TiO ₂	0.28	0.13	78.6	19.0	6.6	1.8
100	Cu/ZrO ₂	0.27	0.14	71.7	28.3	95.7	43.1
	Cu/TiO ₂	0.26	0.12	78.6	19.1	7.0	1.9

selectivity. Consistent agreements between theoretical predictions and experimental observations are achieved. The DFT calculations and in situ DRIFTS measurements observe a significant amount of *HCOO species on both Cu/TiO₂ and Cu/ZrO₂ catalysts during the reaction; however, the production of CH₃OH via the Formate pathway seems not efficient over time due to the poisoning of *HCOO species; by comparison, the RWGS + CO-Hydro pathway via the *H₃CO intermediate is more likely. In terms of catalytic performance, both the DFT calculations and experiments using the steady-state flow reactor demonstrate that ZrO₂ is more effective than TiO₂ to promote the activity and selectivity of CO₂ hydrogenation to CH₃OH on Cu. This is associated with the slightly strengthened interactions with *CO₂, *CO, *HCO, and *H₂CO by taking advantage of the synergy between reduced Zr³⁺ and Cu sites, being strong enough to facilitate the reaction via the RWGS + CO-Hydro pathway, but weak enough to prevent the poisoning of active sites; however, along the Formate pathway more severe surface poisoning by *HCOO is observed. Ideally, the binding property of Cu/oxide catalysts should be tuned selectively, improving the stability of *CO₂, *CO, *HCO, and *H₂CO on Cu, rather than *HCOO, to achieve a high selectivity and yield of CH₃OH.

■ ASSOCIATED CONTENT

■ Supporting Information

The Supporting Information is available free of charge on the ACS Publications website at DOI: 10.1021/jacs.6b05791.

Details of electronic structures and kinetics from both theory and experiment for CO₂ hydrogenation on Cu/oxide catalysts (PDF)

■ AUTHOR INFORMATION

Corresponding Authors

*jgchen@columbia.edu

*pingliu3@bnl.gov

Author Contributions

*S.K. and B.Y. contributed equally to this work and should be regarded as co-first authors.

Notes

The authors declare no competing financial interest.

■ ACKNOWLEDGMENTS

The research was carried out at Brookhaven National Laboratory under Contract DE-SC0012704 with the U.S. Department of Energy, Division of Chemical Sciences. The DFT calculations were performed using computational resources at the Center for Functional Nanomaterials, a user facility at Brookhaven National Laboratory, and at the National Energy Research Scientific Computing Center (NERSC), which is supported by the Office of Science of the U.S. DOE under Contract No. DE-AC02-05CH11231. This research used resources of the Oak Ridge Leadership Computing Facility at the Oak Ridge National Laboratory, which is supported by the Office of Science of the U.S. Department of Energy under Contract No. DE-AC05-00OR22725.

■ REFERENCES

- (1) Graciani, J.; Mudiyansele, K.; Xu, F.; Baber, A. E.; Evans, J.; Senanayake, S. D.; Stacchiola, D. J.; Liu, P.; Hrbek, J.; Sanz, J. F.; Rodriguez, J. A. *Science* **2014**, *345*, 546.
- (2) Park, J. B.; Graciani, J.; Evans, J.; Stacchiola, D.; Senanayake, S. D.; Barrio, L.; Liu, P.; Sanz, J. F.; Hrbek, J.; Rodriguez, J. A. *J. Am. Chem. Soc.* **2010**, *132*, 356.
- (3) Yang, X.; Kattel, S.; Senanayake, S. D.; Boscoboinik, J. A.; Nie, X.; Graciani, J.; Rodriguez, J. A.; Liu, P.; Stacchiola, D. J.; Chen, J. G. *J. Am. Chem. Soc.* **2015**, *137*, 10104.
- (4) Campbell, C. T. *Nat. Chem.* **2012**, *4*, 597.
- (5) Solymsi, F. *J. Catal.* **1985**, *94*, 581.
- (6) Saavedra, J.; Doan, H. A.; Pursell, C. J.; Grabow, L. C.; Chandler, B. D. *Science* **2014**, *345*, 1599.
- (7) Green, I. X.; Tang, W.; Neurock, M.; Yates, J. T. *Science* **2011**, *333*, 736.
- (8) Fu, Q.; Yao, Y.; Guo, X.; Wei, M.; Ning, Y.; Liu, H.; Yang, F.; Liu, Z.; Bao, X. *Phys. Chem. Chem. Phys.* **2013**, *15*, 14708.
- (9) Fu, Q.; Yang, F.; Bao, X. *Acc. Chem. Res.* **2013**, *46*, 1692.
- (10) Fu, Q.; Li, W.-X.; Yao, Y.; Liu, H.; Su, H.-Y.; Ma, D.; Gu, X.-K.; Chen, L.; Wang, Z.; Zhang, H.; Wang, B.; Bao, X. *Science* **2010**, *328*, 1141.
- (11) Willinger, M. G.; Zhang, W.; Bondarchuk, O.; Shaikhtudinov, S.; Freund, H.-J.; Schlögl, R. *Angew. Chem., Int. Ed.* **2014**, *53*, 5998.
- (12) Liu, P. *J. Phys. Chem. C* **2012**, *116*, 25337.
- (13) Porosoff, M. D.; Yan, B. H.; Chen, J. G. *Energy Environ. Sci.* **2016**, *9*, 62.
- (14) Studt, F.; Sharafutdinov, I.; Abild-Pedersen, F.; Elkjaer, C. F.; Hummelshøj, J. S.; Dahl, S.; Chorkendorff, I.; Nørskov, J. K. *Nat. Chem.* **2014**, *6*, 320.
- (15) Nie, X. W.; Esopi, M. R.; Janik, M. J.; Asthagiri, A. *Angew. Chem., Int. Ed.* **2013**, *52*, 2459.

- (16) Behrens, M.; Studt, F.; Kasatkin, I.; Kuhl, S.; Havecker, M.; Abild-Pedersen, F.; Zander, S.; Girgsdies, F.; Kurr, P.; Knief, B. L.; Tovar, M.; Fischer, R. W.; Norskov, J. K.; Schlogl, R. *Science* **2012**, *336*, 893.
- (17) Yang, H. Q.; Xu, Z. H.; Fan, M. H.; Gupta, R.; Slimane, R. B.; Bland, A. E.; Wright, I. *J. Environ. Sci.* **2008**, *20*, 14.
- (18) Kondratenko, E. V.; Mul, G.; Baltrusaitis, J.; Larrazabal, G. O.; Perez-Ramirez, J. *Energy Environ. Sci.* **2013**, *6*, 3112.
- (19) Dorner, R. W.; Hardy, D. R.; Williams, F. W.; Willauer, H. D. *Energy Environ. Sci.* **2010**, *3*, 884.
- (20) Inui, T.; Takeguchi, T. *Catal. Today* **1991**, *10*, 95.
- (21) Aresta, M.; Dibenedetto, A.; Angelini, A. *Chem. Rev.* **2014**, *114*, 1709.
- (22) Centi, G.; Quadrelli, E. A.; Perathoner, S. *Energy Environ. Sci.* **2013**, *6*, 1711.
- (23) Porosoff, M. D.; Yang, X. F.; Boscoboinik, J. A.; Chen, J. G. *Angew. Chem., Int. Ed.* **2014**, *53*, 6705.
- (24) Reske, R.; Duca, M.; Oezaslan, M.; Schouten, K. J. P.; Koper, M. T. M.; Strasser, P. *J. Phys. Chem. Lett.* **2013**, *4*, 2410.
- (25) Reske, R.; Mistry, H.; Behafarid, F.; Cuenya, B. R.; Strasser, P. *J. Am. Chem. Soc.* **2014**, *136*, 6978.
- (26) Rosen, B. A.; Salehi-Khojin, A.; Thorson, M. R.; Zhu, W.; Whipple, D. T.; Kenis, P. J. A.; Masel, R. I. *Science* **2011**, *334*, 643.
- (27) Rasul, S.; Anjum, D. H.; Jedidi, A.; Minenkov, Y.; Cavallo, L.; Takanabe, K. *Angew. Chem., Int. Ed.* **2015**, *54*, 2146.
- (28) Manthiram, K.; Beberwyck, B. J.; Aivisatos, A. P. *J. Am. Chem. Soc.* **2014**, *136*, 13319.
- (29) Waugh, K. C. *Catal. Today* **1992**, *15*, 51.
- (30) Liu, X.; Lu, G. Q.; Yan, Z.; Beltrami, J. *Ind. Eng. Chem. Res.* **2003**, *42*, 6518.
- (31) Yang, Y. X.; Evans, J.; Rodriguez, J. A.; White, M. G.; Liu, P. *Phys. Chem. Chem. Phys.* **2010**, *12*, 9909.
- (32) Yang, Y. X.; White, M. G.; Liu, P. *J. Phys. Chem. C* **2012**, *116*, 248.
- (33) Samson, K.; Śliwa, M.; Socha, R. P.; Góra-Marek, K.; Mucha, D.; Rutkowska-Zbik, D.; Paul, J. F.; Ruggiero-Mikołajczyk, M.; Grabowski, R.; Słoczyński, J. *ACS Catal.* **2014**, *4*, 3730.
- (34) Witoon, T.; Chalorntham, J.; Dumrongbunditkul, P.; Chareonpanich, M.; Limtrakul, J. *Chem. Eng. J.* **2016**, *293*, 327.
- (35) Guo, X.; Mao, D.; Lu, G.; Wang, S.; Wu, G. *J. Catal.* **2010**, *271*, 178.
- (36) Bando, K. K.; Sayama, K.; Kusama, H.; Okabe, K.; Arakawa, H. *Appl. Catal., A* **1997**, *165*, 391.
- (37) Tagawa, T.; Nomura, N.; Shimakage, M.; Goto, S. *Res. Chem. Intermed.* **1995**, *21*, 193.
- (38) Kohn, W.; Sham, L. J. *Phys. Rev.* **1965**, *140*, 1133.
- (39) Hohenberg, P.; Kohn, W. *Phys. Rev.* **1964**, *136*, B864.
- (40) Kresse, G.; Furthmuller, J. *Phys. Rev. B: Condens. Matter Mater. Phys.* **1996**, *54*, 11169.
- (41) Perdew, J. P.; Wang, Y. *Phys. Rev. B: Condens. Matter Mater. Phys.* **1992**, *45*, 13244.
- (42) Kresse, G.; Joubert, D. *Phys. Rev. B: Condens. Matter Mater. Phys.* **1999**, *59*, 1758.
- (43) Blochl, P. E. *Phys. Rev. B: Condens. Matter Mater. Phys.* **1994**, *50*, 17953.
- (44) Monkhorst, H. J.; Pack, J. D. *Phys. Rev. B* **1976**, *13*, 5188.
- (45) Dudarev, S. L.; Botton, G. A.; Savrasov, S. Y.; Humphreys, C. J.; Sutton, A. P. *Phys. Rev. B: Condens. Matter Mater. Phys.* **1998**, *57*, 1505.
- (46) Chrétien, S.; Metiu, H. *J. Phys. Chem. C* **2011**, *115*, 4696.
- (47) Nolan, M. *Chem. Commun.* **2011**, *47*, 8617.
- (48) Henkelman, G.; Uberuaga, B. P.; Jonsson, H. *J. Chem. Phys.* **2000**, *113*, 9901.
- (49) Lunkenbein, T.; Schumann, J.; Behrens, M.; Schlögl, R.; Willinger, M. G. *Angew. Chem., Int. Ed.* **2015**, *54*, 4544.
- (50) Kakumoto, T. *Energy Convers. Manage.* **1995**, *36*, 661.
- (51) Kakumoto, T.; Watanabe, T. *Catal. Today* **1997**, *36*, 39.
- (52) Tang, Q. L.; Hong, Q. J.; Liu, Z. P. *J. Catal.* **2009**, *263*, 114.
- (53) Liu, C.; Yang, B.; Tyo, E.; Seifert, S.; DeBartolo, J.; von Issendorff, B.; Zapol, P.; Vajda, S.; Curtiss, L. A. *J. Am. Chem. Soc.* **2015**, *137*, 8676.
- (54) Campbell, C. T. *Appl. Catal.* **1987**, *32*, 367.
- (55) Yang, Y.; Mims, C. A.; Disselkamp, R. S.; Kwak, J. H.; Peden, C. H. F.; Campbell, C. T. *J. Phys. Chem. C* **2010**, *114*, 17205.
- (56) Yang, Y.; Mims, C. A.; Disselkamp, R. S.; Mei, D.; Kwak, J. H.; Szanyi, J.; Peden, C. H. F.; Campbell, C. T. *Catal. Lett.* **2008**, *125*, 201.
- (57) Yang, Y.; Mims, C. A.; Disselkamp, R. S.; Peden, C. H. F.; Campbell, C. T. *Top. Catal.* **2009**, *52*, 1440.
- (58) Yang, Y.; Mims, C. A.; Mei, D. H.; Peden, C. H. F.; Campbell, C. T. *J. Catal.* **2013**, *298*, 10.
- (59) Peterson, A. A.; Abild-Pedersen, F.; Studt, F.; Rossmeisl, J.; Norskov, J. K. *Energy Environ. Sci.* **2010**, *3*, 1311.
- (60) Grabow, L. C.; Mavrikakis, M. *ACS Catal.* **2011**, *1*, 365.
- (61) Ahouari, H.; Soualah, A.; Le Valant, A.; Pinard, L.; Magnoux, P.; Pouilloux, Y. *React. Kinet., Mech. Catal.* **2013**, *110*, 131.
- (62) Liu, C.; Liu, P. *ACS Catal.* **2015**, *5*, 1004.
- (63) Kattel, S.; Yu, W.; Yang, X.; Yan, B.; Huang, Y.; Wan, W.; Liu, P.; Chen, J. G. *Angew. Chem., Int. Ed.* **2016**, *55*, 7968–7973.
- (64) Sakong, S.; Gross, A. *Surf. Sci.* **2003**, *525*, 107.
- (65) Conner, W. C.; Falconer, J. L. *Chem. Rev.* **1995**, *95*, 759.
- (66) Lukkien, J. J.; Segers, J. P. L.; Hilbers, P. A. J.; Gelten, R. J.; Jansen, A. P. *J. Phys. Rev. E: Stat. Phys., Plasmas, Fluids, Relat. Interdiscip. Top.* **1998**, *58*, 2598.
- (67) Computational Chemistry Comparison and Benchmark Database; <http://cccbdb.nist.gov>.
- (68) Avanesian, T.; Gusmão, G. S.; Christopher, P. *J. Catal.* **2016**, <http://dx.doi.org/10.1016/j.jcat.2016.03.016>.
- (69) Ouyang, F.; Kondo, J. N.; Maruya, K.; Domen, K. *Catal. Lett.* **1998**, *50*, 179.
- (70) Bianchi, D.; Chafik, T.; Khalfallah, M.; Teichner, S. *J. Appl. Catal., A* **1995**, *123*, 89.
- (71) Fisher, I. A.; Bell, A. T. *J. Catal.* **1997**, *172*, 222.
- (72) Bianchi, D.; Chafik, T.; Khalfallah, M.; Teichner, S. *Appl. Catal., A* **1993**, *105*, 223.
- (73) Guglielminotti, E. *Langmuir* **1990**, *6*, 1455.
- (74) Rhodes, M. D.; Pokrovski, K. A.; Bell, A. T. *J. Catal.* **2005**, *233*, 210.
- (75) Turek, A. M.; Wachs, I. E.; Decanio, E. *J. Phys. Chem.* **1992**, *96*, 5000.
- (76) Manzoli, M.; Chiorino, A.; Boccuzzi, F. *Appl. Catal., B* **2005**, *57*, 201.
- (77) Mattsson, A.; Hu, S. L.; Hermansson, K.; Osterlund, L. *J. Chem. Phys.* **2014**, *140*, 034705.
- (78) Arana, J.; Cabo, C. G. I.; Dona-Rodriguez, J. M.; Gonzalez-Diaz, O.; Heffera-Melian, J. A.; Perez-Pena, J. *Appl. Surf. Sci.* **2004**, *239*, 60.
- (79) Bando, K. K.; Sayama, K.; Kusama, H.; Okabe, K.; Arakawa, H. *Appl. Catal., A* **1997**, *165*, 391.
- (80) Tagawa, T.; Nomura, N.; Shimakage, M.; Goto, S. *Res. Chem. Intermed.* **1995**, *21*, 193.
- (81) He, M. Y.; White, J. M.; Ekerdt, J. G. *J. Mol. Catal.* **1985**, *30*, 415.
- (82) Yang, Y.; Evans, J.; Rodriguez, J. A.; White, M. G.; Liu, P. *Phys. Chem. Chem. Phys.* **2010**, *12*, 9909.